A Low Loss Orthogonal Decoupling Magnetic Integrated Structure for Dual Active Bridge Converter

Zhenkai Cao, Wu Chen, *Senior Member, IEEE*, Zhan Shen, *Member, IEEE*, Yichen Chen, Long Jin, Dajun Ma, *Student Member, IEEE*, and Biao Zou

***Abstract*—The volume of magnetic components (transformer and inductor) in a dual active bridge (DAB) converter is a crucial factor determining its power density. This article proposes an orthogonal decoupling magnetic integrated structure (ODMIS) for DAB converter, which aims to reduce the volume of the transformer and inductor. The integrated series inductor and magnetizing inductor do not affect each other in the ODMIS, so the design process of the transformer and inductor can be separated. The condition to realize magnetic circuits decoupling of the transformer and inductor is derived. The loss characteristics of the magnetic core are analyzed, and the optimal decoupling condition to minimize the core loss is also derived. A 400 V/6 kW/20 kHz DAB converter prototype is built to validate the effectiveness of the ODMIS. The measured full-load overall efficiency of the DAB test platform is 97.55%, and the power density of the magnetic integrated components is 10.08 kW/L. Finally, the prototype comparisons between the proposed ODMIS and two existing magnetic integrated structures and discrete magnetic component method are conducted, and the advanced feature of the ODMIS is illustrated.**

***Index Terms*—High-frequency magnetic components, loss characteristic analysis, magnetic circuit orthogonal decoupling, magnetic integrated structure, optimal decoupling condition.**

I. Introduction

DUAL active bridge (DAB) converters are widely used in energy routers [1], uninterruptible power supplies [2], and bidirectional energy storage system [3] due to their features of bidirectional energy flow [4], soft switching [5], and simple structure. DAB converters use high-frequency transformer (HFT) and inductor for the galvanic isolation, voltage conversion, and power transmission [6], [7].

The loss of HFT increases with the frequency due to the eddy current effect of magnetic core, the skin effect, and the proximity effect of winding [8]–[11], [33]. So, the precise modeling of the loss and parasitic are essential for the design and optimization of HFT [34]. The design and optimization of HFT is currently a hot topic. An optimization routine to design a 166 kW/20 kHz HFT prototype by traversing three geometric proportions is presented in [12], and a compact cooling structure including core cooler, winding cooler, and a water-cooled heat sink is designed to realize maximum power density and effective heat dissipation. A 200 kW/15 kHz HFT is designed in [13], and a novel cooling structure that utilizes two layers three-dimensional printed bobbins is adopted to guarantee insulation capability. The design process of a 15 kW/500 kHz HFT is presented in [14], and a new type of composite insulation structure with insulation frame, insulation tape, and epoxy resin potting is proposed to guarantee insulation capability. However, the design process of the above HFT prototypes is only the optimization of a single HFT, and the leakage inductance of the prototypes cannot replace the role of series inductor in actual applications. While, in a DAB converter, the volume and weight of the series inductor cannot be ignored [16]. The magnetic integration combines the HFT and inductor in one structure, which is applied to decrease the passive volume and increase the overall power density.

So far, the magnetic integration can be mainly divided into two categories: using the leakage inductance characteristics of HFT [17]–[20], [24], and restructuring the magnetic core or winding [21]–[23], [25]. For the former one, a magnetic shunt with high permeability is inserted between two halves of an EE core, and the leakage inductance integration is realized by adjusting the width of the air gaps [17], [18]. However, the magnetizing inductance of the integrated structure will be reduced for an air gap introduced into the main magnetic flux path of HFT. In [19], a leakage layer spanning the whole width of the winding window is inserted into the main insulation of the HFT to obtain a larger leakage inductance, while the winding loss is increased 21.7% after integration. Also, this structure is vulnerable to partial discharge due to the incomplete filling of the leakage layer in the main insulation, and the construction of this structure is very complicated for the specific molded

Manuscript received June 7, 2021; revised August 16, 2021 and October 12, 2021; accepted November 28, 2021. Date of publication December 9, 2021; date of current version February 18, 2022. This work was supported in part by the 2020 State Grid Science Technology Project (Research Project: Research on the Key Technologies of High Efficiency and Compact Multi-Port DC Transformer) under Grant SGJSDK00PW2000236, and in part by the National Natural Science Foundation of China under Award 51922028. The design of the magnetic integrated transformer in this article is supported by DMC Co., Ltd., Am Magnetoelectric Technology Co., Ltd., and Hefei Huayao Electronic Industry Co., Ltd. Recommended for publication by Associate Editor M. Chen. (*Corresponding author: Wu Chen*.)

Zhenkai Cao, Wu Chen, Zhan Shen, Yichen Chen, Long Jin, and Dajun Ma are with the School of Electrical Engineering, Southeast University, Nanjing 210096, China (e-mail: caozhenkai@seu.edu.com; chenwu@seu.edu.cn; zhs@seu.edu.cn; chenyichen@seu.edu.cn; jinlong@seu.edu.cn; madajun@seu.edn.cn).

Biao Zou is with Fujian Longking Company, Ltd., Fujian 364412, China (e-mail: 13806997549@139.com).

Color versions of one or more figures in this article are available at https://doi.org/10.1109/TPEL.2021.3133068.

Digital Object Identifier 10.1109/TPEL.2021.3133068

TABLE I
EXISTING MAGNETIC INTEGRATED STRUCTURE SUMMARY

	Leakage layer position	Magnetizing inductance value dropping	Heat dissipation capacity	Size reduction	Loss compared with the discrete version	Integrated structure realization
DTU 2019 [18]	Between two core halves	Yes	Good	20%	N/A	Easy
TU Delft 2006 [19]	In the main insulation	No	Good	N/A	Larger	Difficult
ETH 2012 [20]	Between two core halves	Yes	Good	N/A	N/A	Easy
	On both sides of the core	No	Good	N/A	N/A	Easy
XJTU 2019 [21]	N/A	Yes	Good	8.2%	Larger	Easy
BJTU 2020 [22] (Scheme1)	N/A	Yes	Good	N/A	Larger	Easy
BJTU 2020 [22] (Scheme2)	N/A	Yes	Good	N/A	N/A	Easy
GU 2011 [23] (Vertical integrated structure)	N/A	N/A	Good	N/A	Larger	Easy
GU 2011 [23] (horizontal integrated structure)	N/A	N/A	Poor	N/A	N/A	Difficult
SEU [This article] (ODMIS)	N/A	No	Good	12.1%	Almost the same	Easy

leakage layer adopting Vitroperm powder. Cougo and Kolar proposed two magnetic integration schemes to increase leakage inductance, namely inserting high permeability leakage layers into cut nanocrystalline core, and sticking high permeability leakage layers on both sides of cut nanocrystalline core [20]. The excessive core loss caused by the leakage flux orthogonal to the nanocrystalline lamination is replaced by the core loss caused by the leakage flux in the I-type cores.

For the second type magnetic integration, a reliable integration is realized by wounding the windings of HFT and inductor on the two side columns of EI core, respectively, [21]. However, the magnetizing inductance value reduces 82% due to the introduced air gaps after integration, and the power efficiency drops 3.1% due to the high primary-side current caused by low magnetizing inductance after integration. In [22], two magnetic integration schemes including side columns decoupling integration scheme and multicores integration scheme are introduced. Compared with the former scheme, multicores integration scheme avoids the large core loss and large number of windings. However, the magnetizing inductance is much lower than the discrete scheme due to the air gaps introduced in main and secondary cores. Also, the extra secondary core increases transformer's volume, and based on the core selection in [22], the power density of the integrated prototype reduces 58% compared with side columns decoupling integration scheme. In [23], a horizontal integrated structure is proposed, where both transformer and inductor windings are placed on the same plane by adopting a special constructed core. Compared with the conventional vertical integrated transformers, the magnetic flux of HFT and the inductor does not affect each other, and avoids the decrease of efficiency and excessive temperature rise. However, the heat dissipation of the horizontal integrated structure is difficult due to the smaller contact surface between the winding parts and the air compared with the discrete scheme, and it is difficult to wind the winding on this closed core structure.

According to the above-mentioned analysis, all magnetic integration schemes can replace the discrete magnetic parts. However, magnetizing inductances of most integration schemes are reduced due to the introduced air gaps in the main flux path of the HFT. Also, the heat dissipation capacity and power density of the integrated structure and overall efficiency of the magnetic integrated prototype should be focused. The existing magnetic integrated structure summary is presented in Table I.

This article proposes a low loss orthogonal decoupling magnetic integrated structure (ODMIS) for DAB converter to improve the power density of magnetic components and keep the independence of magnetizing inductance. A rectangular core is used for the HFT, and two spliced I-type cores and part of the rectangular core are adopted for the inductor with distributed air gaps. Compared with [25], the ODMIS is an improvement of the magnetic integrated structure in [25] by conducting two decoupling of the magnetic circuit, which can avoid excessive loss. The novelty of this article can be presented by a thorough comparison between the proposed structure and that shown in [20, Fig. 7(d)], which is shown in Table II.

The rest of this article is organized as follows. Section II introduces the operating principle of DAB converter and two classical magnetic integrated structures. In Section III, the ODMIS is introduced, and the actual inductance matrix along with the decoupling conditions are given through the magnetic circuit model. In Section IV, different decoupling conditions are compared according to the magnetic flux overlap principle, and the optimal decoupling condition is determined to minimize the core loss of integrated magnetic parts. The design process of the ODMIS is presented in Section V. The effectiveness of ODMIS is verified by simulation results in Section VI. In Section VII, experimental results of four prototypes are presented. Finally, Section VIII concludes this article.

TABLE II
COMPARISON BETWEEN THE PROPOSED STRUCTURE AND THE STRUCTURE SHOWN IN [20, FIG. 7(D)]

	Purpose of adding spliced I-type core	Two orthogonal magnetic fluxes	Structure of winding arrangement	Number of the required I-type cores
The structure shown in Fig. 7(d) of [20]	Obtain larger leakage inductance	1) Magnetizing flux of the HFT 2) Leakage flux of the HFT	Separate structure [13]	4
The ODMIS	Form an independent inductor	1) Magnetizing flux of the HFT 2) Integrated inductor flux	Parallel-concentric structure [13]	2

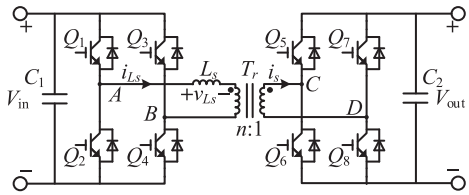

Fig. 1. Topology of the DAB converter.

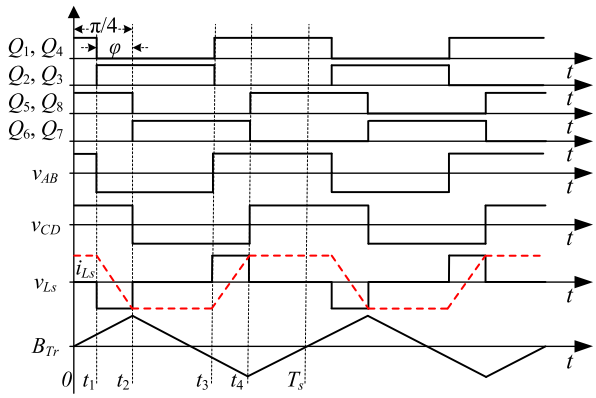

Fig. 2. Typical waveforms of the DAB converter.

II. OPERATING PRINCIPLE OF DAB CONVERTER AND TWO CLASSICAL MAGNETIC INTEGRATED STRUCTURES

A. Operating Principle of DAB Converter

The topology of DAB converter is shown in Fig. 1, which is composed of two full bridges, a series inductor L_s and an HFT T_r. The conventional single-phase-shift control is adopted, and its typical waveforms are shown in Fig. 2, where B_{Tr} is the magnetizing flux density of HFT, $t_1 = (1/4-\varphi/2\pi)T_s$, $t_2 = T_s/4$, $t_3 = (3/4-\varphi/2\pi)T_s$, $t_4 = 3T_s/4$, and φ is the phase-shifted angle and T_s is the switching cycle.

The transmitted power of a DAB converter P_{tran} is as follows:

$$P_{\text{tran}} = \frac{nV_{\text{in}}V_{\text{out}}}{2\pi^2 f_s L_s}\varphi(\pi-\varphi) \tag{1}$$

where n is the turns ratio of primary winding to secondary winding of the HFT, V_{in} and V_{out} are the input voltage and output voltage of the DAB converter, respectively, $f_s = 1/T_s$. According to (1), when V_{in}, V_{out}, and f_s are given, P_{tran} is determined by the inductance value of the series inductor and φ.

B. Two Classical Magnetic Integrated Structures

In [24], the increased leakage inductance of HFT is employed as the series inductor in the DAB converter. This integrated

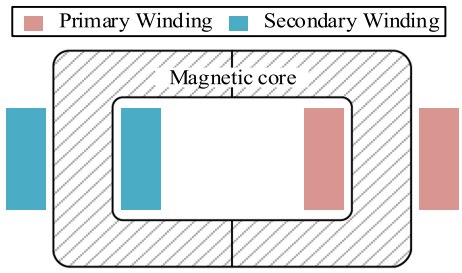

Fig. 3. Large leakage inductance integrated structure.

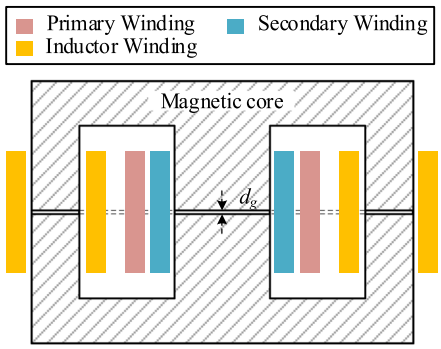

Fig. 4. Decoupling integrated structure in [25].

structure can be applied where a large series inductor is required, as shown in Fig. 3. The primary and secondary windings are wound on the both sides of C-type core separately. The leakage inductance represents the magnetic field energy which is stored in the core window and external space. The magnetic field energy and leakage inductance increase with the distance between windings. However, the magnetic field energy in this structure is distributed not only in the core window area but also in the outer space of the magnetic core. It brings challenge to the theoretical design and accurate calculation of the leakage inductance, and also the electromagnetic interference to other components around it. Moreover, most of the leakage flux generated by the HFT windings passes through the ribbon orthogonally, which remarkably increases the core loss if nanocrystalline-based core is used due to the eddy current effect [20].

In [25], a magnetic decoupling integrated structure is proposed, in which the HFT and inductor winding are wound on the same pair of EE cores, as shown in Fig. 4. d_g is the air gap between two halves of the EE core, which is mainly used to adjust the integrated inductance value. In this structure, the inductor winding directions on both sides are opposite. According to [25], the decoupling between the HFT and inductor can be realized by setting the equal numbers of turns of the inductor windings

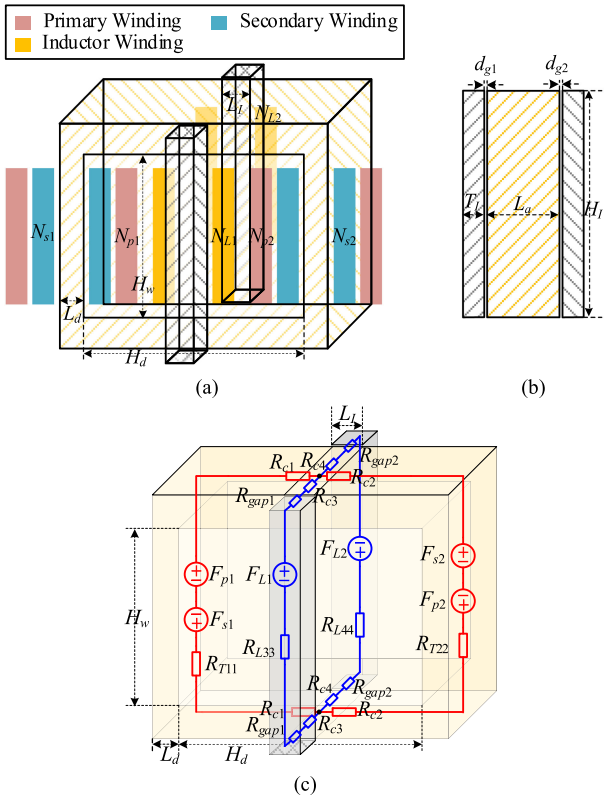

Fig. 5. Core structure and magnetic circuit model of ODMIS. (a) 3-D structure. (b) Right side view. (c) Magnetic circuit model.

on both sides. The air gap inserted into the main magnetic flux path of HFT causes the mutual restriction between the design processes of series inductor and magnetizing inductance, and increases the complexity of the design. In addition, the magnetic flux generated by the HFT and inductor is superimposed on both sides of the EE core, which results in excessive core loss.

III. Orthogonal Decoupling Magnetic Integrated Structure (ODMIS)

A. ODMIS

In order to avoid the shortcomings of above two magnetic integrated structures, this article proposes an ODMIS to separate the magnetic flux paths of the HFT and inductor. The magnetic integrated structure and magnetic circuit diagram of ODMIS are shown in Fig. 5. The main core structure is composed of a rectangular core and two I-type cores. Both the primary and secondary windings of the HFT are divided into two parts with the same proportion, wounded on both the sides of rectangular core with opposite winding directions and then connected in series. The integrated inductor winding is also divided into two parts, which are wound on the two I-type cores with opposite winding directions and then connected in series. Two air gaps with widths of d_{g1} and d_{g2} are inserted between the two I-type cores and rectangular core, respectively, as shown in Fig. 5(b). The width and thickness of rectangular core column are L_d and L_a, respectively, the width and height of core window are H_d and H_w, respectively, the height, width, and thickness of I-type cores are H_I, L_I, and T_I, respectively.

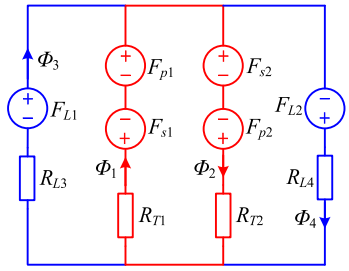

Fig. 6. Simplified magnetic circuit model of the ODMIS.

B. Derivation of the Inductance Matrix of the ODMIS

In Fig. 5(a), the numbers of turns of the primary and secondary windings on the left side column of the rectangular core are N_{p1} and N_{s1}, respectively, and that on the right side column are N_{p2} and N_{s2}, respectively. The number of turns of the inductor winding on the front I-type core is N_{L1}, and that on the back I-type core is N_{L2}. The currents through the primary winding, secondary winding, and inductor winding are i_p, i_s, and i_{Ls}, respectively. The magnetic circuit modeling of ODMIS is established in Fig. 5(c).

In Fig. 5(c), the blue and red parts represent the inductor magnetic circuit and the HFT magnetic circuit, respectively, and the two magnetic circuits are orthogonal to each other. R_{T11} and R_{T22} represent the reluctances of left and right parts of the rectangular core, respectively, R_{L33} and R_{L44} represent the reluctances of front and back I-type cores, respectively, R_{gap1} and R_{gap2} represent the reluctances of air gaps distributed among the front and back I-type cores and the rectangular core, respectively, R_{c1}–R_{c4} represent the reluctances of the core contacting part of the upper and lower iron yokes. For the convenience of analysis, we define $R_{T1} = R_{T11}+2R_{c1}$, $R_{T2} = R_{T22}+2R_{c2}$, $R_{L3} = R_{L33}+2R_{c3}+2R_{gap1}$, and $R_{L4} = R_{L44}+2R_{c4}+2R_{gap2}$, where R_{T1} and R_{T2} represent the total equivalent reluctances of the left and right parts of the rectangular core, respectively, R_{L3} and R_{L4} represent the total equivalent reluctances of the front and back parts of the closed loop path through the I-type cores, respectively. The simplified magnetic circuit model is shown in Fig. 6, where Φ_1 and Φ_2 represent the magnetic flux in the left and right columns of the rectangular core, respectively, Φ_3 and Φ_4 represent the magnetic flux in the front and back I-type cores, respectively.

Based on the magnetic circuit model in Fig. 6, the inductance matrix of ODMIS is derived. The magnetic flux generated by the transformer windings on the left and right sides of the ODMIS (Φ_{T1}, Φ_{T2}) and magnetic flux generated by the inductor windings on the front and back sides of the ODMIS (Φ_{L1}, Φ_{L2}) is derived as follows:

$$\begin{cases} \Phi_{T_1} = \dfrac{(N_{p1}i_p - N_{s1}i_s)(R_{T2}R_{L3}+R_{T2}R_{L4}+R_{L3}R_{L4})}{\Delta} \\ \Phi_{T_2} = \dfrac{(N_{p2}i_p - N_{s2}i_s)(R_{T1}R_{L3}+R_{T1}R_{L4}+R_{L3}R_{L4})}{\Delta} \\ \Phi_{L1} = \dfrac{N_{L1}i_{L_s}(R_{T1}R_{T2}+R_{T1}R_{L4}+R_{T2}R_{L4})}{\Delta} \\ \Phi_{L2} = \dfrac{N_{L2}i_{L_s}(R_{T1}R_{T2}+R_{T1}R_{L3}+R_{T2}R_{L3})}{\Delta} \end{cases} \tag{2}$$

where $\Delta = R_{T1}R_{T2}R_{L3} + R_{T1}R_{T2}R_{L4} + R_{T1}R_{L3}R_{L4} + R_{T2}R_{L3}R_{L4}$.

In addition, Z_1, Z_2, Z_3, and Z_4 is defined as $Z_1 = R_{T2}R_{L3} + R_{T2}R_{L4} + R_{L3}R_{L4}$, $Z_2 = R_{T1}R_{L3} + R_{T1}R_{L4} + R_{L3}R_{L4}$, $Z_3 = R_{T1}R_{T2} + R_{T1}R_{L4} + R_{T2}R_{L4}$, and $Z_4 = R_{T1}R_{T2} + R_{T1}R_{L3} + R_{T2}R_{L3}$.

1) The expressions of magnetic flux corresponding to the four magnetic circuits in Fig. 6 is represented as follows:

$$\begin{cases} \Phi_1 = \Phi_{T1} + \Phi_{T2}\frac{R_{L3}R_{L4}}{Z_2} - \Phi_{L1}\frac{R_{T2}R_{L4}}{Z_3} \\ \quad +\Phi_{L2}\frac{R_{T2}R_{L3}}{Z_4} \\ \Phi_2 = \Phi_{T1}\frac{R_{L3}R_{L4}}{Z_1} + \Phi_{T2} + \Phi_{L1}\frac{R_{T1}R_{L4}}{Z_3} \\ \quad -\Phi_{L2}\frac{R_{T1}R_{L3}}{Z_4} \\ \Phi_3 = -\Phi_{T1}\frac{R_{T2}R_{L4}}{Z_1} + \Phi_{T2}\frac{R_{T1}R_{L4}}{Z_2} + \Phi_{L1} \\ \quad +\Phi_{L2}\frac{R_{T1}R_{T2}}{Z_4}. \\ \Phi_4 = \Phi_{T1}\frac{R_{T2}R_{L3}}{Z_1} - \Phi_{T2}\frac{R_{T1}R_{L3}}{Z_2} + \Phi_{L1}\frac{R_{T1}R_{T2}}{Z_3} \\ \quad +\Phi_{L2}. \end{cases} \tag{3}$$

According to Faraday electromagnetic induction principle, the transformer and inductor winding voltages is as follows:

$$\begin{cases} V_p = N_{p1}\frac{d\Phi_1}{dt} + N_{p2}\frac{d\Phi_2}{dt} \\ V_s = -N_{s1}\frac{d\Phi_1}{dt} - N_{s2}\frac{d\Phi_2}{dt} \\ V_{L_s} = N_{L1}\frac{d\Phi_3}{dt} + N_{L2}\frac{d\Phi_4}{dt}. \end{cases} \tag{4}$$

The self-inductance and mutual-inductance can be represented as follows:

$$\begin{bmatrix} V_{L_s} \\ V_p \\ V_s \end{bmatrix} = \begin{bmatrix} L_s & M_{pL_s} & M_{sL_s} \\ M_{pL_s} & L_{pri} & -M_{ps} \\ M_{sL_s} & -M_{ps} & L_{\mathrm{sec}} \end{bmatrix} \begin{bmatrix} di_{L_s}/dt \\ di_p/\mathrm{d}t \\ \mathrm{d}i_s/\mathrm{d}t \end{bmatrix}. \tag{5}$$

Then, the integrated inductance L_s can be solved as follows:

$$L_s = N_{L1}^2\frac{Z_3}{\Delta} + N_{L2}^2\frac{Z_4}{\Delta} + 2N_{L1}N_{L2}\frac{R_{T1}R_{T2}}{\Delta}. \tag{6}$$

And the analytical formula of the magnetizing inductance in the ODMIS can be solved as follows:

$$L_m = N_{p1}^2\frac{Z_1}{\Delta} + N_{p2}^2\frac{Z_2}{\Delta} + 2N_{p1}N_{p2}\frac{R_{L3}R_{L4}}{\Delta}. \tag{7}$$

The expressions of mutual-inductance between transformer winding and inductor winding are as follows:

$$\begin{cases} M_{pL_s} = \frac{(N_{p1}R_{T2} - N_{p2}R_{T1})(N_{L2}R_{L3} - N_{L1}R_{L4})}{\Delta} \\ M_{sL_s} = \frac{(N_{s2}R_{T1} - N_{s1}R_{T2})(N_{L2}R_{L3} - N_{L1}R_{L4})}{\Delta} \end{cases} \tag{8}$$

where M_{pLs} represents the mutual-inductance between the primary winding and inductor winding, M_{sLs} represents the mutual-inductance between the secondary winding and inductor winding. It can be seen from (8) that in order to realize the electrical decoupling between the transformer and inductor, at least one of the following two decoupling conditions needs to be satisfied:

$$N_{p1}R_{T2} = N_{p2}R_{T1}\mathrm{AND}N_{s1}R_{T2} = N_{s2}R_{T1} \tag{9}$$

$$N_{L2}R_{L3} = N_{L1}R_{L4}. \tag{10}$$

If the turns ratio of N_{p1} to N_{p2} AND the turns ratio of N_{s1} to N_{s2} are equal to the ratio of R_{T1} to R_{T2}, or the turns ratio of N_{L1} to N_{L2} is equal to the ratio of R_{L3} to R_{L4}, the electrical parameters decoupling of the HFT and the integrated inductor in the ODMIS can be realized. Compared with the decoupling integrated structure in Fig. 4, the air gap is arranged out of the rectangular core in the ODMIS, so limitation of the magnetizing inductance by the air gap is eliminated.

IV. Loss Characteristics Analysis of ODMIS

The decoupling conditions of ODMIS ensure the electrical parameters independence of the HFT and inductor. Moreover, it is important to assess the loss of magnetic components after the integration. The winding loss of ODMIS is related to the current, frequency, number of turns, and the cross-sectional area dimensions of the rectangular core and I-type cores. In a specific design process where the rectangular core and I-type cores have been determined, we consider that the magnetic flux generated by inductor winding is constant. Then, the total turns number of the inductor winding is fixed. Therefore, winding loss of the ODMIS approximately remains constant as the design parameters change, and the core loss is a more powerful factor in terms of total loss. Next, the influence of design parameters on the core loss adopting the ODMIS is analyzed in this section.

A. High-Frequency Core Loss Algorithm

For a DAB converter, the voltages across the inductor and the HFT are nonsinusoidal waves. Therefore, the improved generalized Steinmetz equation (IGSE) is used for the core loss calculation [26]. The expression of IGSE algorithm is shown in the following equations:

$$P_v = \frac{1}{T_s}\int_0^{T_s} k_i\left|\frac{dB(t)}{dt}\right|^{\alpha}|\Delta B|^{\beta-\alpha}dt \tag{11}$$

$$k_i = K\left(2^{\beta+1}\pi^{\alpha-1}\left(0.2761 + \frac{1.7061}{\alpha+1.354}\right)\right)^{-1} \tag{12}$$

where P_v represents the core loss per unit volume, d$B(t)$/dt represents the magnetic flux density change rate, ΔB represents the peak-to-peak value of magnetic flux density in an operating period, and K, α, β represent the three coefficients of the Steinmetz equation, respectively, which are obtained by fitting the measured core loss data under sinusoidal excitation.

B. Analysis of Magnetic Flux Overlap Phenomenon Under Different Decoupling Conditions

1) Only the first decoupling condition in (9) is satisfied.

In this case, the flux offset $\Delta\Phi_1$ between Φ_1 and Φ_2 in the main magnetic circuit of HFT can be expressed as follows (13):

$$\Delta\Phi_1 = \frac{i_{L_s}(R_{T1}+R_{T2})}{\Delta}\cdot(N_{L2}R_{L3} - N_{L1}R_{L4}) + \frac{R_{L3}+R_{L4}}{\Delta}\cdot \left[i_p\left(N_{p1}R_{T2} - N_{p2}R_{T1}\right) - i_s\left(N_{s1}R_{T2} - N_{s2}R_{T1}\right)\right]. \tag{13}$$

According to (9), the second term of $\Delta\Phi_1$ is zero.

In this case, the flux offset $\Delta\Phi_2$ between Φ_3 and Φ_4 in the main magnetic circuit of the integrated inductor can be expressed

as follows:

$$\Delta\Phi_2 = \frac{i_{Ls}(R_{T1}+R_{T2})}{\Delta}\cdot(N_{L1}R_{L4}-N_{L2}R_{L3}) - \frac{R_{L3}+R_{L4}}{\Delta}\cdot \left[i_p\left(N_{p1}R_{T2}-N_{p2}R_{T1}\right) - i_s\left(N_{s1}R_{T2}-N_{s2}R_{T1}\right)\right]. \tag{14}$$

From (13) and (14), the magnetic flux offset of the main magnetic circuit of HFT and integrated inductor is not zero, that is, magnetic flux overlap occurs in the core.

2) Only the second decoupling condition in (10) is satisfied.

In this case, since the HFT windings are divided into two parts with equal proportion and distributed on both sides of the rectangular core, it can be deduced from (13) and (14) that both $\Delta\Phi_1$ and $\Delta\Phi_2$ are zero. Therefore, there is no magnetic flux overlap in the core, and the magnetic flux paths of HFT and inductor are separated from each other.

3) Both the decoupling conditions in (9) and (10) are satisfied.

In this case, it can be deduced from (13) and (14) that both $\Delta\Phi_1$ and $\Delta\Phi_2$ are zero. The magnetic flux paths of HFT and inductor are separated from each other, and there is no magnetic flux overlap phenomenon.

In general, when the decoupling condition in (10) is satisfied, the magnetic parts after integration can be equivalent to discrete magnetic parts for loss analysis.

C. Optimal Decoupling Condition of the ODMIS

In the DAB converter application, the expressions of the magnetic flux density of each magnetic circuit are provided in (15) to analyze the influence of design parameters on the core loss of integrated magnetic parts, where B_1 and B_2 are the magnetic flux densities in the left and right columns of the rectangular core, respectively, B_3 and B_4 are the magnetic flux densities in the front and back I-type cores, respectively, B_{Tr} is the magnetizing flux density of HFT in the ODMIS, A_{eT} is the area of the rectangular core column, and A_{eL} is the area of I-type core column. The expressions of magnetizing flux density and inductor current are shown in (16) and (17), where $N_s = N_{s1}+N_{s2}$ represents the total number of secondary winding turns in the ODMIS

$$\begin{cases} B_1 = \frac{i_{Ls}R_{T2}(N_{L2}R_{L3}-N_{L1}R_{L4})}{\Delta\cdot A_{eT}} + B_{Tr} \\ B_2 = \frac{i_{Ls}R_{T1}(N_{L1}R_{L4}-N_{L2}R_{L3})}{\Delta\cdot A_{eT}} + B_{Tr} \\ B_3 = \frac{(N_{L1}+N_{L2})i_{Ls}R_{T1}R_{T2}}{\Delta\cdot A_{eL}} + \frac{N_{L1}i_{Ls}R_{L4}(R_{T1}+R_{T2})}{\Delta\cdot A_{eL}} \\ B_4 = \frac{(N_{L1}+N_{L2})i_{Ls}R_{T1}R_{T2}}{\Delta\cdot A_{eL}} + \frac{N_{L2}i_{Ls}R_{L3}(R_{T1}+R_{T2})}{\Delta\cdot A_{eL}}. \end{cases} \tag{15}$$

In order to find the decoupling condition that minimizes the overall core loss, core loss analysis of the rectangular core and the two I-type cores are carried out, respectively. In this section, the core loss is analyzed with a piecewise linear model [27].

1) Core loss analysis of rectangular core

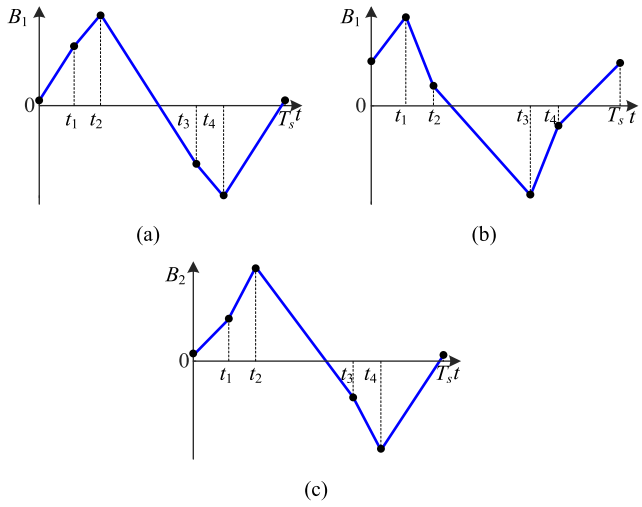

Fig. 7. Magnetic flux density waveforms in the rectangular core. (a) Waveform of the magnetic flux density in the left column of the rectangular core when $V_{\text{out}}/N_s \geq 2x_1(V_{\text{in}}/L_s)$. (b) Waveform of the magnetic flux density in the left column of the rectangular core when $V_{\text{out}}/N_s < 2x_1(V_{\text{in}}/L_s)$. (c) Waveform of the magnetic flux density in the right column of the rectangular core.

According to (15)–(17), the waveforms of the magnetic flux densities B_1 and B_2 can be obtained in Fig. 7

$$B_{Tr} = \begin{cases} \frac{V_{\text{out}}}{N_s\cdot A_{eT}}t, & t\in[0,t_2) \\ \frac{V_{\text{out}}}{N_s\cdot A_{eT}}\left(\frac{1}{2}T_s - t\right), & t\in[t_2,t_4) \\ \frac{V_{\text{out}}}{N_s\cdot A_{eT}}\left(t-T_s\right), & t\in[t_4,T_s] \end{cases} \tag{16}$$

$$i_{L_s} = \begin{cases} \frac{V_{\text{in}}\varphi T_s}{2\pi L_s}, & t\in[0,t_1) \\ \frac{V_{\text{in}}}{L_s}\left[\left(\frac{1}{2}-\frac{\varphi}{2\pi}\right)T_s - 2t\right], & t\in[t_1,t_2) \\ -\frac{V_{\text{in}}\varphi T_s}{2\pi L_s}, & t\in[t_2,t_3) \\ \frac{V_{\text{in}}}{L_s}\left[\left(\frac{\varphi}{2\pi}-\frac{3}{2}\right)T_s + 2t\right], & t\in[t_3,t_4) \\ \frac{V_{\text{in}}\varphi T_s}{2\pi L_s}, & t\in[t_4,T_s]. \end{cases} \tag{17}$$

Two variables are defined as $x_1 = R_{T2}(N_{L2}R_{L3}-N_{L1}R_{L4})/\Delta$ and $x_2 = R_{T1}(N_{L2}R_{L3}-N_{L1}R_{L4})/\Delta$. A hypothesis that $N_{L2}R_{L3}\geq N_{L1}R_{L4}$ is made during analysis. In the case of Fig. 7(a), the maximum and minimum values of B_1 appear at t_2 and t_4, respectively. And in the case of Fig. 7(b), the maximum and minimum values of B_1 appear at t_1 and t_3, respectively. The maximum and minimum values of B_2 always appear at t_2 and t_4, respectively. Next, the rectangular core loss corresponding to the two cases will be analyzed.

Define that the core volumes of the left and right parts of the rectangular core are V_1 and V_2, respectively.

In the case of $V_{\text{out}}/N_s \geq 2x_1(V_{\text{in}}/L_s)$, the core loss expression of the rectangular core is shown in (18) at the bottom of the next page, where k_{i1}, α_1, β_1 are obtained from the rectangular core loss data. It can be deduced from (18), $P_{\text{coreloss }Tr}$ increases with x_1. Therefore, only when $x_1 = 0$, that is, when $N_{L2}R_{L3} = N_{L1}R_{L4}$, the rectangular core has the smallest core loss.

In the case of $V_{\text{out}}/N_s < 2x_1(V_{\text{in}}/L_s)$, the core loss expression of the rectangular core is shown in (19) at the bottom of this page.

It can be deduced from (19), $P_{\mathrm{coreloss}\,Tr}$ increases with x_1. Therefore, when $x_1 = L_s/2nN_s$, the rectangular core has the smallest core loss. Moreover, because $P_{\mathrm{coreloss}\,Tr}$ is a piecewise continuous function with $x_1 = L_s/2nN_s$ as the separation point, to minimize the core loss of the rectangular core, $N_{L2}R_{L3} = N_{L1}R_{L4}$ should be satisfied.

2) Core loss analysis of I-type core

Considering that the reluctance of the air gaps inserted between the two I-type cores and the rectangular core is much greater than that of the cores, that is R_{L3}, $R_{L4} >> R_{T1}$, R_{T2}, dividing the numerator and denominator of (15) by $R_{L3}R_{L4}$, B_3 and B_4 can be transformed into the following:

$$\begin{cases} B_3 = \left[\frac{(N_{L1}+N_{L2})R_{T1}R_{T2}}{(R_{T1}+R_{T2})R_{L3}R_{L4}} + \frac{N_{L1}}{R_{L3}}\right]\frac{i_{L_s}}{A_{eL}} \\ B_4 = \left[\frac{(N_{L1}+N_{L2})R_{T1}R_{T2}}{(R_{T1}+R_{T2})R_{L3}R_{L4}} + \frac{N_{L2}}{R_{L4}}\right]\frac{i_{L_s}}{A_{eL}}. \end{cases} \tag{20}$$

The first part of B_3 and B_4 is negligible because it is tiny compared to the second part. Therefore, (20) can be further simplified as follows:

$$\begin{cases} B_3 = N_{L1}i_{L_s}/R_{L3}A_{eL} \\ B_4 = N_{L2}i_{L_s}/R_{L4}A_{eL}. \end{cases} \tag{21}$$

It can be seen that the magnetic flux density waveforms in the two I-type cores are proportional to the inductor current. Assuming that the volumes of the front and back I-type cores are V_3 and V_4, respectively, and $V_3 = V_4$, the core loss expression of the I-type cores is shown in the following:

$$P_{\mathrm{coreloss}L} = \frac{k_{i2}2^{\alpha_2}}{f_s^{\beta_2-\alpha_2}}\left(\frac{\varphi}{\pi}\right)^{\beta_2-\alpha_2+1}\left(\frac{V_{\mathrm{in}}}{L_sA_{eL}}\right)^{\beta_2}\cdot \left[\left(\frac{N_{L1}}{R_{L3}}\right)^{\beta_2} + \left(\frac{N_{L2}}{R_{L4}}\right)^{\beta_2}\right]V_3 \tag{22}$$

where k_{i2}, α_2, and β_2 are obtained from the I-type core loss data.

Derived from the aforementioned inductance matrix, (23) can be obtained, where the numerator and denominator of (6) are divided by $R_{L3}R_{L4}$

$$L_s = N_{L2}^2\frac{1}{R_{L4}} + N_{L1}^2\frac{1}{R_{L3}} + 2N_{L1}N_{L2}\frac{R_{T1}R_{T2}}{(R_{T1}+R_{T2})R_{L3}R_{L4}}. \tag{23}$$

Since R_{L3}, $R_{L4} >> R_{T1}$, R_{T2}, the third term of (23) can be ignored, and (23) can be expressed as follows:

$$\frac{N_{L2}^2}{R_{L4}} + \frac{N_{L1}^2}{R_{L3}} = L_s. \tag{24}$$

Define that $a_3 = 1/R_{L3}$, $a_4 = 1/R_{L4}$, then $P_{\mathrm{coreloss}L}$ in (22) is taken a derivative concerning a_3 to obtain the following:

$$\frac{dP_{\mathrm{coreloss}L}}{da_3} = k_{i2}2^{\alpha_2}\frac{\varphi}{\pi}\left(\frac{\varphi}{\pi f_s}\right)^{\beta_2-\alpha_2}\left(\frac{V_{\mathrm{in}}}{L_sA_e}\right)^{\beta_2}V_3\beta_2N_{L1}\cdot \left[(N_{L1}a_3)^{\beta_2-1} - \frac{N_{L1}}{N_{L2}}\left(\frac{L_s-N_{L1}^2a_3}{N_{L2}}\right)^{\beta_2-1}\right]. \tag{25}$$

In order to find the point corresponding to the least loss, the zero point of (25) should be determined to obtain the minimum point of $P_{\mathrm{coreloss}L}$. In this case, a_3 and a_4 are expressed in the following equation:

$$\begin{cases} a_3 = L_sN_{L1}^{\frac{2-\beta_2}{\beta_2-1}} \Big/ \left(N_{L1}^{\frac{\beta_2}{\beta_2-1}} + N_{L2}^{\frac{\beta_2}{\beta_2-1}}\right) \\ a_4 = L_sN_{L2}^{\frac{2-\beta_2}{\beta_2-1}} \Big/ \left(N_{L1}^{\frac{\beta_2}{\beta_2-1}} + N_{L2}^{\frac{\beta_2}{\beta_2-1}}\right). \end{cases} \tag{26}$$

In the design procedure, the turns of the front and back inductor windings are the same, that is $N_{L1} = N_{L2}$. In order to minimize the core loss of the I-type cores, $N_{L2}R_{L3} = N_{L1}R_{L4}$ should be satisfied, which can be seen from (24) and (26). Therefore, $N_{L2}R_{L3} = N_{L1}R_{L4}$ is the optimal decoupling condition of the ODMIS. That is, the I-type cores are arranged symmetrically, and the inductor windings are evenly distributed. That is to say, the total loss of integrated magnetic parts is minimized when there is no magnetic flux overlap. Under the optimal decoupling condition, magnetic flux paths of the HFT and the inductor are orthogonal to each other and separated from each other. Therefore, both the HFT and inductor can be designed separately.

V. Design Process of the ODMIS

The design process of the ODMIS will be illustrated in this section and the parameters of DAB converter are shown in Table III.

A. Core Material Selection

Nanocrystalline alloys are widely used in the frequency range of 1 to 25 kHz due to its better loss characteristics and higher saturation flux density [8]. Therefore, nanocrystalline is chosen as the rectangular core material.

$$\begin{aligned} P_{\mathrm{coreloss}Tr} = {} & f_s\left(\frac{V_{\mathrm{out}}}{2N_sf_sA_{eT}} - x_1\frac{V_{\mathrm{in}}\varphi}{\pi L_sf_sA_{eT}}\right)^{\beta_1-\alpha_1}k_{i1}\left[\left(\frac{V_{\mathrm{out}}}{N_s\cdot A_{eT}}\right)^{\alpha_1}\frac{2\pi-2\varphi}{2\pi f_s} + \left(\frac{V_{\mathrm{out}}}{N_s\cdot A_{eT}} - x_1\frac{2V_{\mathrm{in}}}{L_sA_{eT}}\right)^{\alpha_1}\frac{2\varphi}{2\pi f_s}\right]V_1 \\ & + f_s\left(\frac{V_{\mathrm{out}}}{2N_sf_sA_{eT}} + x_2\frac{V_{\mathrm{in}}\varphi}{\pi L_sf_sA_{eT}}\right)^{\beta_1-\alpha_1}k_{i1}\left[\left(\frac{V_{\mathrm{out}}}{N_s\cdot A_{eT}}\right)^{\alpha_1}\frac{2\pi-2\varphi}{2\pi f_s} + \left(\frac{V_{\mathrm{out}}}{N_s\cdot A_{eT}} + x_2\frac{2V_{\mathrm{in}}}{L_sA_{eT}}\right)^{\alpha_1}\frac{2\varphi}{2\pi f_s}\right]V_2 \end{aligned} \tag{18}$$

$$\begin{aligned} P_{\mathrm{coreloss}Tr} = {} & f_s\left(\frac{V_{\mathrm{out}}(\pi-2\varphi)}{2\pi N_sf_sA_{eL}} + x_1\frac{V_{\mathrm{in}}\varphi}{\pi L_sf_sA_{eL}}\right)^{\beta_1-\alpha_1}k_{i1}\left[\left(\frac{V_{\mathrm{out}}}{N_s\cdot A_{eL}}\right)^{\alpha_1}\frac{2\pi-2\varphi}{2\pi f_s} + \left(x_1\frac{2V_{\mathrm{in}}}{L_sA_{eL}} - \frac{V_{\mathrm{out}}}{N_s\cdot A_{eL}}\right)^{\alpha_1}\frac{2\varphi}{2\pi f_s}\right]V_1 \\ & + f_s\left(\frac{V_{\mathrm{out}}}{2N_sf_sA_{eL}} + x_2\frac{V_{\mathrm{in}}\varphi}{\pi L_sf_sA_{eL}}\right)^{\beta_1-\alpha_1}k_{i1}\left[\left(\frac{V_{\mathrm{out}}}{N_s\cdot A_{eL}}\right)^{\alpha_1}\frac{2\pi-2\varphi}{2\pi f_s} + \left(\frac{V_{\mathrm{out}}}{N_s\cdot A_{eL}} + x_2\frac{2V_{\mathrm{in}}}{L_sA_{eL}}\right)^{\alpha_1}\frac{2\varphi}{2\pi f_s}\right]V_2 \end{aligned} \tag{19}$$

TABLE III
PARAMETER OF DAB CONVERTER

Parameter	Value
Rated power P_t	6kW
Input voltage V_{in}	400V
Output voltage V_o	400V
Series inductor L_s	105μH
Operating frequency f_s	20kHz

In actual production, nanocrystalline can be made into I-type core by cutting a raw rectangular nanocrystalline ribbon. However, the cutting will cause a larger loss due to more surface short circuits, and wasting of the material will occur because the rest of the raw rectangular nanocrystalline ribbon is difficult to reuse [28]. Therefore, the more accessible ferrite is used as a spliced I-type core material.

B. Winding Selection

In order to reduce winding loss of the ODMIS in high-frequency applications, Litz wire is adopted as the winding material.

As shown in Table III, the operation frequency of the DAB converter is 20 kHz. The corresponding skin effect depth is as follows:

$$\delta_0=\sqrt{\frac{1}{\mu_0\pi f_s\sigma}}=0.467\,\text{mm} \tag{27}$$

where μ_0 represents the permeability of air and σ represents the conductivity of copper. In order to reduce the influence of the skin effect and proximity effect on the ac winding loss, the Litz wire with a diameter of 0.1 mm is selected. Considering the maximum current density of 6 A/mm^2, the strand number of litz wire is selected as 350.

C. Specification of the HFT

In order to obtain a larger magnetizing inductance, the AM-120×105×40 cut nanocrystalline core from AMMET is adopted for the rectangular core [29], and the number of transformer winding turns is set as 24. In this occasion, the peak magnetizing flux density of transformer is 0.22 T, which is less than the saturation flux density of nanocrystalline. The material specifications of this cut nanocrystalline core is shown in Table IV. The parallel-concentric winding structure is selected as the HFT winding structure due to the least leakage inductance [13].

D. Specification of the Integrated Inductor

The cross-sectional area dimensions of the spliced I-type core is selected as 20 mm×15 mm that represents L_I×T_I for minimizing the dimension of I-type core. It can be seen from the specification of transformer, the heigh of the I-type core should be 105 mm. The T15×20×105 ferrite core from DMC is used for the two I-type cores [30], and DMR95 is chosen as the core material. The material specifications of this I-type core is shown in Table IV.

TABLE IV
MATERIAL SPECIFICATIONS

Parameter	Value	
	nanocrystalline	DMR95
Steinmetz parameter K	1.848	0.0386
Steinmetz parameter α	1.39	1.781
Steinmetz parameter β	2.094	2.419
Saturation flux density B_{sat}	1.2T	0.53T
Relative permeability	10000	3300

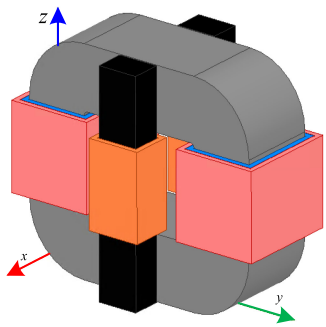

Fig. 8. Simulation model of the magnetic integrated transformer and inductor.

In the ODMIS, the expressions of peak flux density in I-type core is shown in (28) when the optimal decoupling condition is satisfied

$$B_{L\max}=\frac{V_{\text{in}}\cdot\varphi}{2\pi N_L L_I T_I f_s} \tag{28}$$

where $N_L = N_{L1}+N_{L2}$, and $B_{L\max}$ should be smaller than saturation flux density of the I-type core material. Therefore, The peak flux density in I-type core is set as 0.36 T, and N_L is selected as 18.

E. Air Gap Width Selection

After determining the dimensions of the I-type cores and the turns number of inductor winding, d_{g1} and d_{g2} should be determined to obtain a target inductance value. According to (6), the width of air gaps is adjusted to 0.65 mm, that is, $d_{g1} = d_{g2} = 0.65$ mm.

VI. FINITE-ELEMENT SIMULATION VERIFICATION

The designed parameters of the magnetic integrated transformer and inductor with ODMIS are shown in Table V, and its simulation model is shown in Fig. 8. The finite-element simulation is conducted in ANSYS software.

A. Simulation of Integrated Transformer Decoupling Situation

Current excitation is applied to the HFT winding and the inductor winding in the Maxwell eddy current field based on

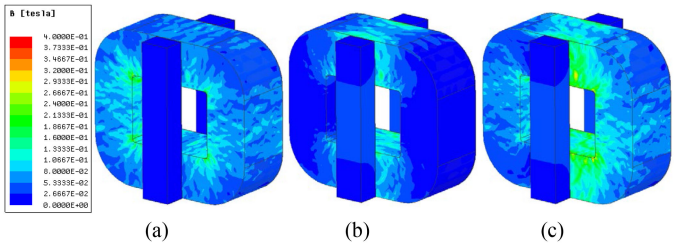

Fig. 9. Magnetic density distribution in the magnetic core under different conditions. (a) Current excitation is only applied to the HFT winding. (b) Current excitation is only applied to the inductor winding. (c) Current excitation is applied to HFT winding and inductor winding simultaneously.

ANSYS software, and Fig. 9 shows the obtained magnetic flux density distribution diagram. It can be seen in Fig. 9(a) that when the current excitation is only applied to the HFT winding, the flux density is distributed in the rectangular core, and there is no flux density distributed in the I-type cores. In Fig. 9(b), when the current excitation is only applied to the inductor winding, there is no flux density distributed in the two columns of the rectangular core. The flux density is distributed in the core contacting part of upper and lower iron yokes of the rectangular core and I-type cores. In the two cases, it is well verified that the decoupling between the magnetic flux paths of HFT and the inductor is realized. In Fig. 9(c), when the current excitation is applied to HFT winding and inductor winding simultaneously, the flux density in the iron yoke of the rectangular core is higher than that in other parts of the core. It is because of the orthogonal superposition of the inductor flux and the transformer flux in this part.

Moreover, the mutual inductance between the HFT windings and the inductor winding is obtained. The mutual inductances between the primary/secondary windings and the inductor winding are 0.224 and 0.225 μH, respectively, which are negligible compared with the integrated inductance 105.85 μH. Therefore, this magnetic integrated transformer can realize electrical decoupling between the HFT and inductor.

B. Simulation of Operating Performance of the ODMIS

The simulation of the operating performance of the ODMIS is carried out in the Maxwell transient field based on ANSYS software, and an external circuit is built to apply excitation to the windings of the integrated magnetic parts. In this case, the waveforms of current flowing through the integrated inductor and voltage across it are shown in Fig. 10.

The simulated waveforms in Fig. 10 are consistent with the theoretical waveforms shown in Fig. 2, which indicates that the proposed ODMIS has the same function as the discrete magnetic parts in a DAB converter. The simulated flux density waveform in the left column of the rectangular core is shown in Fig. 11(a). It can be seen that the flux density waveform in the left column of the rectangular core is the same as the flux density of the HFT in Fig. 2.

In order to verify the three situations in Fig. 7 when the optimal decoupling condition is not satisfied, two sets of air gap size are selected. The two sets of air gaps are $d_{g1} = 0.8$ mm,

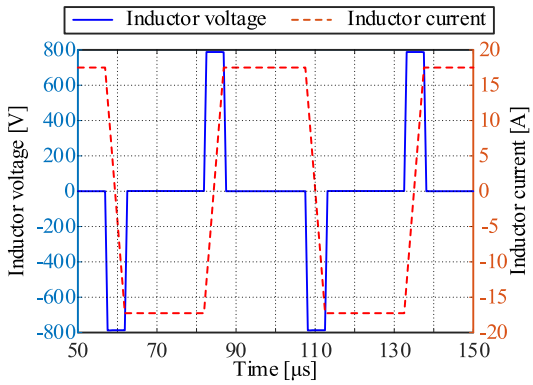

Fig. 10. Simulation results of the integrated inductor.

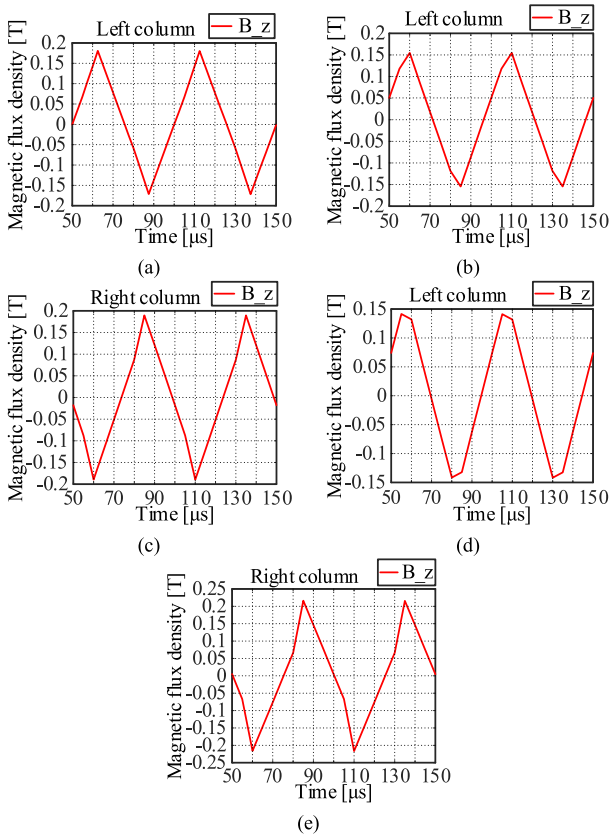

Fig. 11. Magnetic flux density waveform of each part of the rectangular core under different situations. (a) Left column when $d_{g1} = 0.65$ mm and $d_{g2} = 0.65$ mm. (b) Left column when $d_{g1} = 0.8$ mm and $d_{g2} = 0.5$ mm. (c) Right column when $d_{g1} = 0.8$ mm and $d_{g2} = 0.5$ mm. (d) Left column when $d_{g1} = 1.5$ mm and $d_{g2} = 0.4$ mm. (e) Right column when $d_{g1} = 1.5$ mm and $d_{g2} = 0.4$ mm.

$d_{g2} = 0.5$ mm, and $d_{g1} = 1.5$ mm, $d_{g2} = 0.4$ mm, which are corresponding to the two cases of $V_{\text{out}}/N_s \geq 2x_1(V_{\text{in}}/L_s)$ and $V_{\text{out}}/N_s < 2x_1(V_{\text{in}}/L_s)$, respectively. Fig. 11(b)–(e) shows the flux density waveforms of the two cases. When $d_{g1} = 0.8$ mm and $d_{g2} = 0.5$ mm, the waveform in Fig. 11(b) is consistent with the theoretical waveform shown in Fig. 7(a). When $d_{g1} = 1.5$ mm and $d_{g2} = 0.4$ mm, the waveform in Fig. 11(d) is consistent with the theoretical waveform shown in Fig. 7(b). Also, the waveforms in Fig. 11(c) and (e) are consistent with

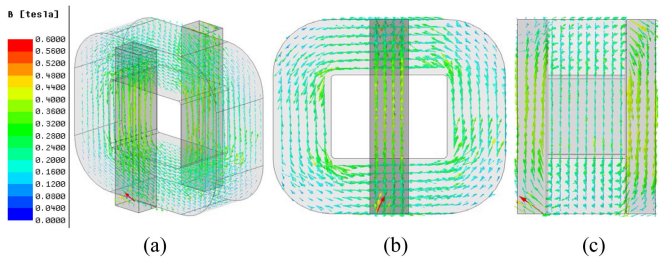

Fig. 12. Vector diagram of magnetic flux density in the ODMIS when $d_{g1} = 0.65$ mm and $d_{g2} = 0.65$ mm viewed from different directions. (a) Full view. (b) Front view. (c) Right view.

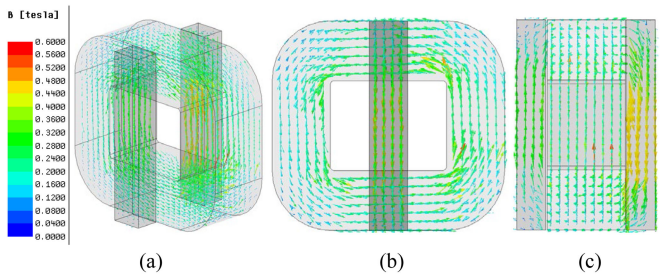

Fig. 13. Vector diagram of magnetic flux density in the ODMIS when $d_{g1} = 0.8$ mm and $d_{g2} = 0.5$ mm viewed from different directions. (a) Full view. (b) Front view. (c) Right view.

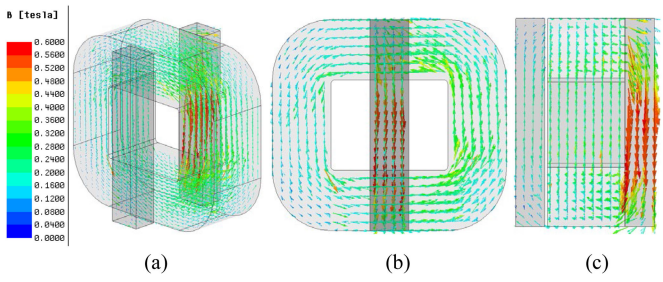

Fig. 14. Vector diagram of magnetic flux density in the ODMIS when $d_{g1} = 1.5$ mm and $d_{g2} = 0.4$ mm viewed from different directions. (a) Full view. (b) Front view. (c) Right view.

the theoretical waveform shown in Fig. 7(c). The simulated waveforms in Fig. 11 verify the rationality of the derivation process of optimal decoupling condition in Section IV.

The vector diagrams of flux density in the ODMIS when $d_{g1} = 0.65$ mm and $d_{g2} = 0.65$ mm, $d_{g1} = 0.8$ mm and $d_{g2} = 0.5$ mm, $d_{g1} = 1.5$ mm, and $d_{g2} = 0.4$ mm are simulated in the transient field, and the results are shown in Figs. 12 –14, respectively.

From Figs. 12–14, it can be seen that magnetic flux overlap phenomenon will occur when the optimal decoupling condition is not satisfied.

From Section IV-C, it can be seen that (9) is not necessarily to be satisfied on the basis of satisfying the optimal decoupling conditions, that is there are no restrictions on the design and optimization of the HFT when ODMIS is actually adopted. In order to verify the above conclusion, two change schemes are designed on the basis of the prototype shown in Fig. 8. In scheme 1, the change is to set $N_{p1} = N_{s1} = 8$ and $N_{p2} = N_{s2} = 16$. In scheme 2, the change is that move the pair of I-type cores 5 mm to the left along the nanocrystalline core. The vector diagrams

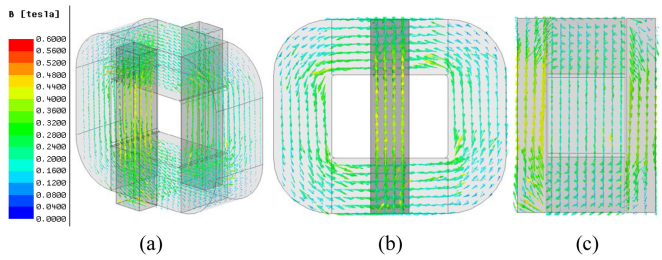

Fig. 15. Vector diagram of magnetic flux density of scheme 1, where $N_{p1} = N_{s1} = 8$ and $N_{p2} = N_{s2} = 16$ viewed from different directions. (a) Full view. (b) Front view. (c) Right view.

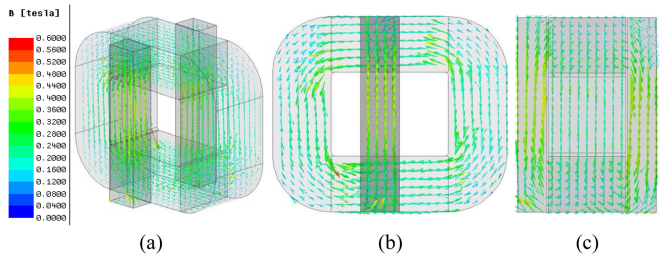

Fig. 16. Vector diagram of magnetic flux density of scheme 2 where I-type cores are moved 5 mm left along the rectangular core viewed from different directions. (a) Full view. (b) Front view. (c) Right view.

TABLE V
PARAMETERS OF THE ODMIS PROTOTYPE

Rectangular core material	Nanocrystalline	I-Type core material	Ferrite
N_{p1}	12	N_{p2}	12
N_{s1}	12	N_{s2}	12
N_{L1}	9	N_{L2}	9
$L_d \times L_a$	30mm×40mm	$H_d \times H_w$	60mm×45mm
$L_l \times T_l$	20mm×15mm	H_l	105mm
Winding current density	5.46A/mm^2	d_{g1}, d_{g2}	0.65mm, 0.65mm

of flux density of the two schemes are shown in Figs. 15 and 16, respectively.

From Figs. 15 and 16, it can be seen that there is no magnetic flux overlap phenomenon even when (9) is not satisfied.

The transient field simulation results of the ODMIS such as core loss of the structure and magnetic flux distribution in the core are listed in Table VI.

According to Table VI, the magnetic flux overlap phenomenon will become more serious with a larger deviation between d_{g1} and d_{g2}, which will bring about a substantial increase in core loss. Thus, the optimal decoupling condition in Section IV-C is vital for uniform flux density distribution and minimizing core losses. However, when (9) is not satisfied, the simulated flux density distributions in Figs. 15 and 16 are almost the same as that in Fig. 12, which confirms that whether the decoupling condition (9) is satisfied does not affect the performance of the ODMIS. Also, the three cases have the similar core loss, which confirms that whether (9) is satisfied does not affect the core loss of the structure.

In order to give a more explicit illustration of the effect of superimposed magnetic flux on the core loss, the top views of

TABLE VI
TRANSIENT FIELD SIMULATION RESULTS

Air gaps arrangement	Corresponding case	Core loss	Magnetic flux distribution
d_{g1}=0.65mm, d_{g2}=0.65mm	x_1=0, shown in Fig. 12	34W	No magnetic flux overlapping
d_{g1}=0.8mm, d_{g2}=0.5mm	$V_{out}/N_s \geq 2x_1(V_{in}/L_s)$, and $x_1 \neq 0$, shown in Fig. 13	35.65W	Slight magnetic flux overlapping
d_{g1}=1.5mm, d_{g2}=0.4mm	$V_{out}/N_s < 2x_1(V_{in}/L_s)$, shown in Fig. 14	41.36W	Serious magnetic flux overlapping
d_{g1}=0.65mm, d_{g2}=0.65mm	x_1=0, N_{p1}= N_{s1}=8, N_{p2}= N_{s2}=16, shown in Fig. 15	34.12W	No magnetic flux overlapping
d_{g1}=0.65mm, d_{g2}=0.65mm	x_1=0, 5mm moving left of I core, shown in Fig. 16	34.09W	No magnetic flux overlapping

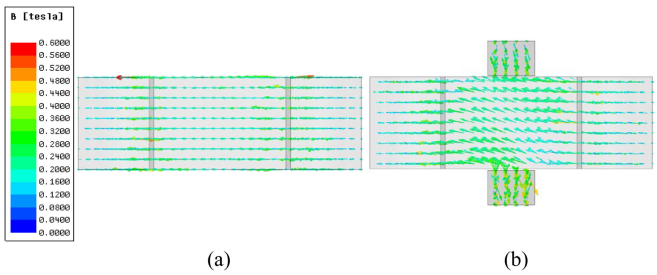

Fig. 17. Top view of the vector diagram of magnetic flux density before and after integration when $d_{g1} = 0.65$ mm and $d_{g2} = 0.65$ mm. (a) Before integration. (b) After integration.

the vector diagram of magnetic flux density before and after integration are shown in Fig. 17(a)and (b), respectively. And the core loss of the nanocrystalline core before and after integration are simulated as 12.83 and 14.85 W, respectively.

It can be seen from Fig. 17 that the amplitude of the flux density in the iron yoke of the nanocrystalline core after integration is almost the same as that of the flux density before integration. And, the increasement of core loss after integration is much smaller than the core loss before integration. During the actual design, the flux density in the nanocrystalline core can be set larger than that in the I-type ferrite core due to its higher saturation flux density. In this case, the effect of the superimposed magnetic flux on the core loss of the original discrete solution can be further ignored.

VII. EXPERIMENTAL VERIFICATION

A. Prototype Adopting the ODMIS

A DAB converter prototype with the parameters in Table V was built, and the MOSFET of IPW60R070CFD7 from *Infineon Technology* [31] is selected as the switches Q_1–Q_8. The prototype adopting the ODMIS is designed according to the design

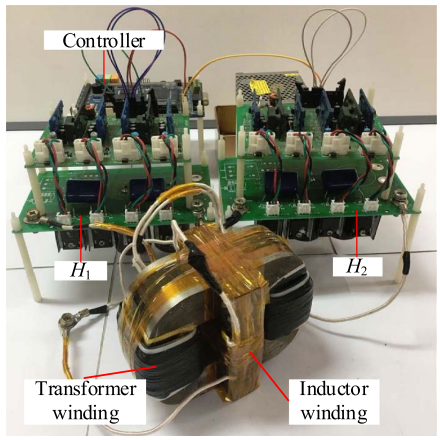

Fig. 18. DAB converter test platform and magnetic integrated prototype.

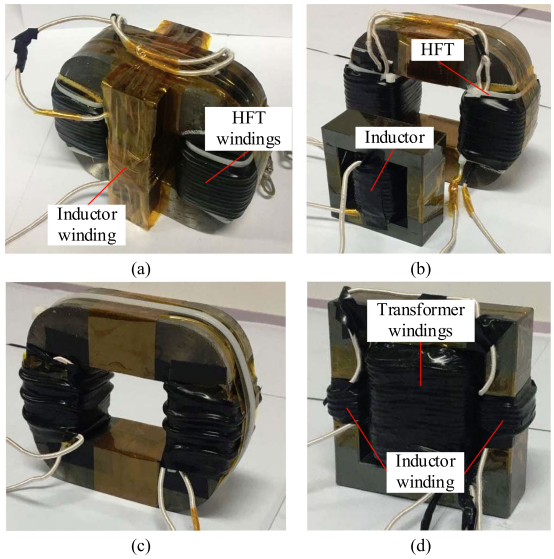

Fig. 19. Test prototypes adopting the four structures. (a) ODMIS. (b) Discrete magnetic parts. (c) Large leakage inductance integrated structure in Fig. 3. (d) Decoupling integrated structure in Fig. 4.

process in Section V. In the prototype, and the isolation between the I-type ferrite cores and the nanocrystalline core adopts 13 layers of 0.05 mm polyimide film. Litz wire of 0.1 mm×350 strands is used for both the HFT winding and inductor winding, and the HFT secondary winding is close to the core, while the primary winding is wound on the secondary one. The insulation between the secondary winding and the nanocrystalline core uses two layers of 0.05 mm polyimide film.

The main insulation between the primary and secondary windings and the insulation between the inductor winding and ferrite core use 4 layers of 0.05 mm polyimide film. The test platform is shown in Fig. 18, and the magnetic integrated prototype is shown in Fig. 19(a).

The LCR bridge tester YB2811 is used to measure the inductance parameters of the prototype, and the results are shown in Table VII. L_k is the leakage inductance, L_m is the magnetizing inductance, and L_s is the integrated inductor. According to the test results in Table VII, the decoupling between the HFT and the

TABLE VII
MEASURED INDUCTANCES OF THE FOUR PROTOTYPES SHOWN IN FIG. 19

	ODMIS		Discrete magnetic parts		Large leakage inductance integrated structure	Decoupling integrated structure
	rectangular core	I-type core	HFT core	Inductor core		
Core material	nanocrystalline	DMR95	nanocrystalline	DMR95	nanocrystalline	DMR95

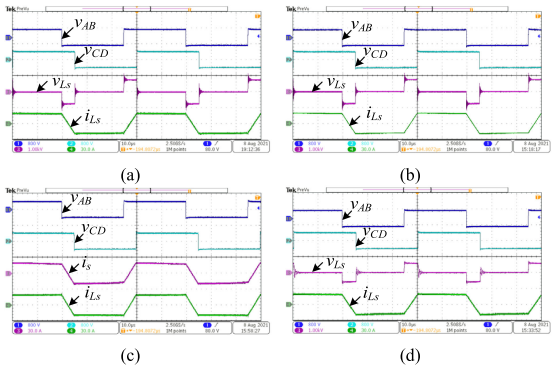

Fig. 20. Experimental results with the four prototypes. (a) ODMIS. (b) Discrete magnetic parts. (c) Large leakage inductance integrated structure in Fig. 3. (d) Decoupling integrated structure in Fig. 4.

inductor of the prototype is achieved, and the mutual inductance almost does not influence the converter operation.

The key waveforms of the magnetic integrated DAB converter under full-load conditions are shown in Fig. 20(a). The experimental waveforms are similar to the theoretical waveforms in Fig. 2, which indicates that the electrical parameters of this magnetic integrated transformer prototype are reliable. The conversion efficiency of the magnetic integrated.

DAB converter under full load condition is measured as 97.55% by adopting power analyzers YOKOGAWA WT1800E.

B. Prototypes Adopting Other Structures

In order to illustrate the advantages of the proposed ODMIS, three prototypes with the discrete magnetic parts, the large leakage inductance integrated structure in Fig. 3 and the decoupling integrated structure in Fig. 4 are designed and compared. Considering that the integration idea of ODMIS is to replace the discrete inductor core by splicing two I-type cores while keeping the original discrete HFT unchanged. Then, an E70/33/32 ferrite core is adopted for the discrete inductor, the winding is 10 turns, and an air gap of 0.45 mm is cushioned between two halves of the EE core. The measured inductance value is 100.74 μH, and the prototype is shown in Fig. 19(b). For the large leakage inductance integrated prototype, the main core still adopts AM-120×105×40 cut nanocrystalline core, the number of HFT winding turns is 15. The primary winding is wound on the left column, while the secondary winding is wound on the right column, the measured leakage inductance is 102 μH, and the prototype is shown in Fig. 19(c). In the third prototype, an EE110/56/36 ferrite core is selected as the main core, and an air gap of 0.45mm separates two halves of the EE core. In this structure, the transformer windings are wound with 40 turns which are divided into two successive layers on the central column of the EE core, and the inductor winding is wound with 8 turns, which are arranged equally on both columns and connected in series, and the third prototype is shown in Fig. 19(d). The measured inductances of the four prototypes are shown in Table VII, and the core materials adopted by the four prototypes are shown in Table VIII.

TABLE VIII
CORE MATERIALS OF THE FOUR PROTOTYPES

Parameters	Inductance values			
	ODMIS	Discrete magnetic parts	Large leakage inductance integrated structure	Decoupling integrated structure
L_k	5.2μH	5.2μH	102μH	29.24μH
L_s	103.75μH	100.74μH	/	75μH
M_{pLs}	1.5μH	0μH	/	4μH
M_{sLs}	0.75μH	0μH	/	4.25μH
L_m	17.5mH	16.157mH	5.876mH	2.706 mH

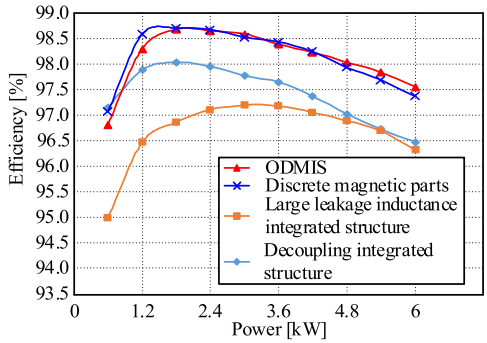

Fig. 21. Overall efficiency curves of four prototypes.

The experimental results are shown in Fig. 20. It can be seen that all three prototypes can guarantee the normal operation of DAB converter. Moreover, the measured full-load overall conversion efficiencies of the three DAB converter prototypes are 97.37%, 96.32%, and 96.47%, respectively.

C. Efficiency Comparison

The overall efficiency curves of the DAB converter with four different magnetic components are provided in Fig. 21, where the load changes from 10% to 100% rated power. It can be seen that the overall efficiency of the prototype which adopts the ODMIS is closest to that of the discrete magnetic parts, which indicates that the ODMIS does not increase loss after integration.

The overall efficiency of the prototype adopting the large leakage inductance integrated structure is the lowest, which is because the leakage flux generated by the HFT is orthogonal to the nanocrystalline ribbon, which causes the core loss to increase significantly. The efficiency of the prototype using the

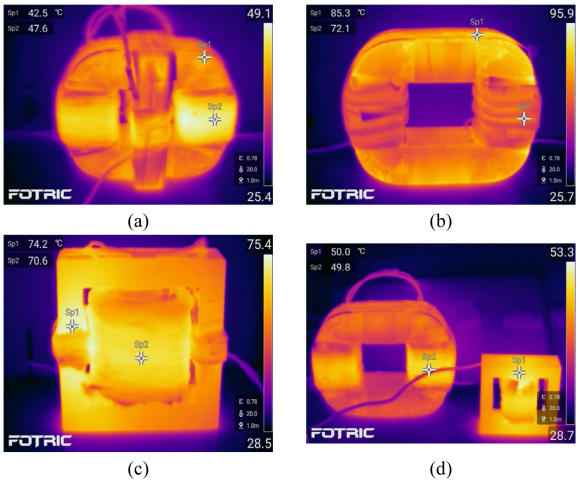

Fig. 22. Thermal imaging pictures of different prototypes in the steady state. (a) ODMIS. (b) Large leakage inductance integrated structure. (c) Decoupling integrated structure. (d) Discrete magnetic parts.

decoupling integrated structure is also lower than that adopting the ODMIS and discrete magnetics parts in most load conditions, which is due to the increase of core loss caused by the superposition of magnetic fluxes, and the considerable winding loss caused by the successive winding in two layers of the HFT windings [32].

D. Thermal Verification

A FOTRIC infrared thermal imaging camera is used to compare the temperature rise of the prototypes at half-load adopting the ODMIS, the large leakage inductance integrated structure, the decoupling integrated structure, and the discrete magnetic parts. The thermal imaging pictures are shown in Fig. 22, where S_{p1} and S_{p2} represent the highest temperature rise of core and winding, respectively. From Fig. 22(a), the highest temperature rise of the prototype adopting the ODMIS in steady state is 22.2 K, which appears in the winding part, and the temperature rise of the core part is lower than 20 K. In addition, the temperature rise in Fig. 22(a) is evenly distributed. On the contrary, from Fig. 22(b), the highest temperature rise of the prototype using the large leakage inductance integrated structure is 59.6 K, which appears in the outer laminated part of the nanocrystalline core. This phenomenon confirms that the orthogonal magnetic flux can increase core loss. From Fig. 22(c), the highest temperature rise of the prototype using the decoupling integrated structure is 45.7 K, which appears in the left column of the EE core, and the temperature rise in the winding part is also high, which reaches 42.1 K. So, the superposition of magnetic flux in the left column will increase the core loss, and the winding loss caused by the proximity effect is also significant.

From Fig. 22(d), the highest temperature rise of the discrete prototype in steady state is 21.3 K. From the comparison, the prototypes using the ODMIS and the discrete magnetic parts have the lowest temperature rise.

E. Power Density Comparison

The power density of the prototypes with ODMIS and discrete magnetic parts is measured and compared. As for the ODMIS, the volume and weight are measured as 0.595 L and 3 kg, respectively. Therefore, the power density can be calculated as 10.08 kW/L. As for the discrete prototype, the volume and weight are measured as 0.677 L and 3.2 kg, respectively. Then, the power density is calculated as 8.862 kW/L. The volume and weight of the magnetic parts with the application of ODMIS reduce 12.1% and 6.3%, respectively, and the power density is increased by 13.8%. When calculating the volume and the power density of the magnetic parts, the core, winding, and core window area are taken into consideration at the same time. The weight measurement of the magnetic parts before and after integration takes the cores and windings into consideration at the same time.

A thorough power density comparison is shown in Table IX. It can be seen from Table IX that power densities of the large leakage inductance integrated structure and the decoupling integrated structure are higher than that of the ODMIS. However, the losses of the large leakage inductance integrated structure and the decoupling integrated structure are much larger than that of the ODMIS.

Considering of reasonable cooling measures, some additional devices for heat dissipation will reduce the actual power density of the large leakage inductance integrated structure and the decoupling integrated structure, and result in greater loss of the magnetic parts [12]. Therefore, the advantages of the two magnetic integrated structures in power density will be further weakened, and the disadvantages in efficiency will be further amplified after considering actual cooling measures. On the contrary, the ODMIS increases the power density further on the premise of keeping the loss of the magnetic parts at the same level as that of the discrete solution. After comprehensive consideration, ODMIS proposed in this article is superior to the other two magnetic integrated structures.

F. Loss Breakdown of the Four Prototypes

Based on the parameter in Table III, the loss breakdown of the DAB converter adopting the four structures is simulated. PLECS is employed to simulate the power loss of the switches and the dc-link capacitors, and ANSYS is employed to simulated the power loss of the four prototypes including winding loss and core loss. The switches adopted in the DAB converter is IPW60R070CFD7 from *Infineon Technology* [31].

The summarized values for simulated losses in the DAB converter adopting the four structures including the ODMIS, the discrete magnetic parts, the large leakage inductance integrated structure, and the decoupling integrated structure are shown in Fig. 23. It can be seen that the losses on the circuit including conduction loss, switching loss, and capacitors loss of the four schemes are similar, the major difference of the four schemes is the loss of the magnetic parts including winding loss and core loss. From Fig. 23, it can be seen that the loss distribution of two schemes adopting the ODMIS and the discrete magnetic parts are almost the same. In terms of the large leakage inductance integrated structure, even though its winding loss is slightly less

TABLE IX
THOROUGH POWER DENSITY COMPARISON AMONG FOUR PROTOTYPES

	Full load overall efficiency	Volume/L	Weight/kg	Power density/kW/L
This work (ODMIS)	97.55%	0.595	3	10.081
Discrete magnetic parts	97.37%	0.677	3.2	8.862
Large leakage inductance integrated structure.	96.32%	0.524	2.45	11.46
Decoupling integrated structure	96.47%	0.335	2.15	17.889

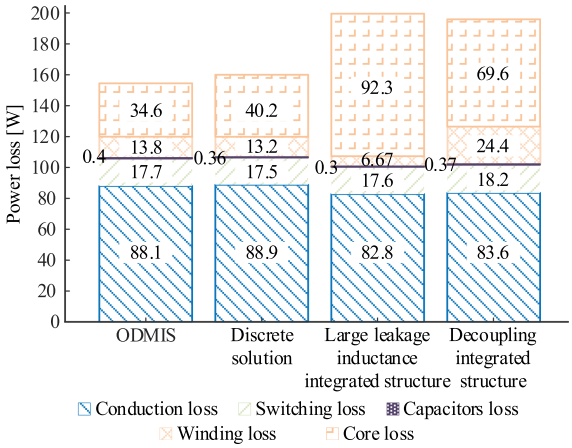

Fig. 23. Loss comparison of the four schemes which adopt the ODMIS, the discrete magnetic parts, the large leakage inductance integrated structure and the decoupling integrated structure.

than that of the ODMIS, its core loss is much larger than that of the ODMIS. In terms of the decoupling integrated structure, both the winding loss and the core loss of it are much larger than that of the ODMIS.

Therefore, the ODMIS is suitable for the DAB converter due to the loss consistency before and after integration, while the large leakage inductance integrated structure and the decoupling integrated structure are not suitable for the integrated DAB converter for the large increase of magnetic parts loss.

VIII. CONCLUSION

This article proposes a low loss ODMIS for the DAB converter. It improves the power density while maintains the magnetizing inductance compared with the discrete magnetic solutions. The decoupling conditions and loss characteristics of the ODMIS are analyzed in detail. Then, the optimal decoupling condition is obtained, where the I-type cores are arranged symmetrically, and the integrated inductor windings are distributed evenly. Moreover, the magnetic flux paths of HFT and the integrated inductor in the ODMIS are separated, the core loss after integration is optimized, and the overall efficiency of the DAB converter adopting the ODMIS is kept at the same level as the discrete magnetic solutions. Finally, the effectiveness of the ODMIS is verified through finite-element simulation and experimental results.

REFERENCES

[1] B. Zhou, X. Yang, R. Nong, Z. Li, T. Q. Zheng, and P. Kobrle, "Multi-objective optimization control for input-series output-parallel dual-active-bridge DC-DC converter in EER application," in *Proc. IEEE Int. Power Electron. Motion Control Conf.*, 2020, pp. 2408–2413.

[2] B. L. Narasimharaju, V. V. Prahlad, U. R. Reddy, K. V. Babu, and P. Srinivasan, "Optimized dual active bridge bi-directional DC-DC converter for UPS application," in *Proc. Int. Conf. Power Electron., Drives Energy Syst.*, 2014, pp. 1–6.

[3] F. Xue, R. Yu, and A. Q. Huang, "A 98.3% efficient GaN isolated bidirectional DC–DC converter for DC microgrid energy storage system applications," *IEEE Trans. Ind. Electron.*, vol. 64, no. 11, pp. 9094–9103, Nov. 2017.

[4] P. He and A. Khaligh, "Comprehensive analyses and comparison of 1 kW isolated DC–DC converters for bidirectional EV charging systems," *IEEE Trans. Transport. Electrific.*, vol. 3, no. 1, pp. 147–156, Mar. 2017.

[5] M. Yaqoob, K. H. Loo, and Y. M. Lai, "Extension of soft-switching region of dual-active-bridge converter by a tunable resonant tank," *IEEE Trans. Power Electron.*, vol. 32, no. 12, pp. 9093–9104, Dec. 2017.

[6] G. Ortiz, J. Biela, D. Bortis, and J. W. Kolar, "1 megawatt, 20 kHz, isolated, bidirectional 12kV to 1.2kV DC-DC converter for renewable energy applications," in *Proc. Int. Power Electron. Conf.-ECCE Asia*, 2010, pp. 3212–3219.

[7] L. Shu, W. Chen, and Z. Song, "Prediction method of DC bias in DC-DC dual-active-bridge converter," *CPSS Trans. Power Electron. Appl.*, vol. 4, no. 2, pp. 152–162, Jun. 2019.

[8] I. Villar, "Multiphysical characterization of medium-frequency power electronic transformers," Ph.D. dissertation, École Polytechnique Fédérale de Lausanne, Ind. Electron. Lab., EPFL Lausanne, Lausanne, Switzerland, 2010.

[9] J. Muhlethaler, J. Biela, J. W. Kolar, and A. Ecklebe, "Improved core-loss calculation for magnetic components employed in power electronic systems," *IEEE Trans. Power Electron.*, vol. 27, no. 2, pp. 964–973, Feb. 2012.

[10] W. G. Hurley, W. H. Wolfle, and J. G. Breslin, "Optimized transformer design: Inclusive of high-frequency effects," *IEEE Trans. Power Electron.*, vol. 13, no. 4, pp. 651–659, Jul. 1998.

[11] K. Zhang *et al.*, "Accurate calculation and sensitivity analysis of leakage inductance of high-frequency transformer with litz wire winding," *IEEE Trans. Power Electron.*, vol. 35, no. 4, pp. 3951–3962, Apr. 2020.

[12] M. Leibl, G. Ortiz, and J. W. Kolar, "Design and experimental analysis of a medium-frequency transformer for solid-state transformer applications," *IEEE Trans. Emerg. Sel. Topics Power Electron.*, vol. 5, no. 1, pp. 110–123, Mar. 2017.

[13] Z. Guo, R. Yu, W. Xu, X. Feng, and A. Q. Huang, "Design and optimization of a 200-kW medium-frequency transformer for medium voltage SiC PV inverters," *IEEE Trans. Power Electron.*, vol. 36, no. 9, pp. 10548–10560, Sep. 2021.

[14] S. Zhao, Q. Li, F. C. Lee, and B. Li, "High-frequency transformer design for modular power conversion from medium-voltage AC to 400 VDC," *IEEE Trans. Power Electron.*, vol. 33, no. 9, pp. 7545–7557, Sep. 2018.

[15] T. Guillod and J. W. Kolar, "Medium-frequency transformer scaling laws: Derivation, verification, and critical analysis," *CPSS Trans. Power Electron. Appl.*, vol. 5, no. 1, pp. 18–33, Mar. 2020.

[16] H. J. Choi, B. G. Seo, M. H. Ryu, Y. P. Cho, and J. H. Jung, "Effective magnetic component design of three-phase dual-active-bridge converter for LVDC distribution system," *IEEE Trans. Ind. Electron.*, vol. 68, no. 3, pp. 1828–1840, Mar. 2021.

[17] M. Meinhardt, M. Duffy, T. O'Donnell, S. O'Reilly, J. Flannery, and C. O. Mathuna, "New method for integration of resonant inductor and transformer-design, realisation, measurements," in *Proc. IEEE Appl. Power Electron. Conf. Expo.*, 1999, pp. 1168–1174.

[18] M. Li, Z. Ouyang, and M. A. E. Andersen, "High-frequency LLC resonant converter with magnetic shunt integrated planar transformer," *IEEE Trans. Power Electron.*, vol. 34, no. 3, pp. 2405–2415, Mar. 2019.

[19] M. Pavlovsky, S. W. H. de Haan, and J. A. Ferreira, "Winding losses in high-current, high-frequency transformer foil windings with leakage layer," in *Proc. PESC Rec. IEEE Annu. Power Electron. Spec. Conf.*, 2006, pp. 1–7.

[20] B. Cougo and J. W. Kolar, "Integration of leakage inductance in tape wound core transformers for dual active bridge converters," in *Proc. Int. Conf. Integr. Power Electron. Syst.*, 2012, pp. 1–6.

[21] S. Wang, D. Yuan, A. Wang, K. Liu, H. Li, and S. Wang, "Circuit-field coupling and magnetic-thermal coupling analysis of RRF converter designed with magnetic integration," *IEEE Trans. Magn.*, vol. 55, no. 5, pp. 1–8, May 2019.
[22] J. Wang *et al.*, "Design of integrated magnetic transformer for high frequency LLC converter," in *Proc. Int. Conf. HVDC*, 2020, pp. 986–991.
[23] S. Stegen and J. Lu, "Structure comparison of high-frequency planar power integrated magnetic circuits," *IEEE Trans. Magn.*, vol. 47, no. 10, pp. 4425–4428, Oct. 2011.
[24] X. Li, W. Huang, B. Cui, and X. Jiang, "Inductance characteristics of the high-frequency transformer in dual active bridge converters," in *Proc. Int. Conf. Elect. Mach. Syst.*, 2019, pp. 1–5.
[25] S. Gao and Z. Zhao, "Magnetic integrated LLC resonant converter based on independent inductance winding," *IEEE Access*, vol. 9, pp. 660–672, 2021, doi: 10.1109/ACCESS.2020.3046616.
[26] K. Venkatachalam, C. R. Sullivan, T. Abdallah, and H. Tacca, "Accurate prediction of ferrite core loss with nonsinusoidal waveforms using only steinmetz parameters," in *Proc. IEEE Workshop Comput. Power Electron.*, 2002, pp. 36–41.
[27] I. Villar, U. Viscarret, I. Etxeberria-Otadui, and A. Rufer, "Global loss evaluation methods for nonsinusoidally fed medium-frequency power transformers," *IEEE Trans. Ind. Electron.*, vol. 56, no. 10, pp. 4132–4140, Oct. 2009.
[28] B. Cougo, A. Tuysüz, J. Mühlethaler, and J. W. Kolar, "Increase of tape wound core losses due to interlamination short circuits and orthogonal flux components," in *Proc. 37th Annu. Conf. IEEE Ind. Electron. Soc.*, 2011, pp. 1372–1377.
[29] Shenzhen Advanced Metal Magnetic-Electronic Technology Co., Ltd., 2021. [Online]. Available: http://www.ammet.com.cn
[30] DMC Co., Ltd., 2021. [Online]. Available: http://www.chinadmegc.com
[31] Infineon Technology, 2021. [Online]. Available: https://www.infineon.com
[32] R. P. Wojda and M. K. Kazimierczuk, "Winding resistance and power loss of inductors with litz and solid-round wires," *IEEE Trans. Ind. Appl.*, vol. 54, no. 4, pp. 3548–3557, Jul./Aug. 2018.
[33] Z. Shen *et al.*, "The faraday shields loss of transformers," *IEEE Trans. Power Electron.*, vol. 35, no. 11, pp. 12194–12206, Nov. 2020.
[34] Z. Shen, H. Wang, Y. Shen, Z. Qin, and F. Blaabjerg, "An improved stray capacitance model for inductors," *IEEE Trans. Power Electron.*, vol. 34, no. 11, pp. 11153–11170, Nov. 2019.

Zhenkai Cao was born in Jiangsu, China, in 1997. He received the B.S. degree in electrical engineering and its automation from Soochow University, Jiangsu, China, in 2019. He is currently working toward the M.S. degree in electrical engineering from Southeast University, Nanjing, China.

His research interests include high-power high-frequency transformer model and design, and magnetic integration scheme.

Wu Chen (Senior Member, IEEE) was born in Jiangsu, China, in 1981. He received the B.S., M.S., and Ph.D. degrees in electrical engineering from the Nanjing University of Aeronautics and Astronautics, Nanjing, China, in 2003, 2006, and 2009, respectively.

From 2009 to 2010, he was a Senior Research Assistant with the Department of Electronic Engineering, City University of Hong Kong, Kowloon, Hong Kong. In 2010–2011, he was a Postdoctoral Researcher with Future Electric Energy Delivery and Management Systems Center, North Carolina State University, Raleigh. Since September 2011, he has been an Associate Research Fellow with the School of Electrical Engineering, Southeast University, Nanjing, where he has been a Professor since 2016. His main research interests include soft-switching converters, power delivery, and power electronic system integration.

Dr. Chen serves as an Associate Editor for the IEEE TRANSACTIONS ON INDUSTRIAL ELECTRONICS, *Journal of Power Electronics*, and *CPSS Transactions on Power Electronics and Applications*.

Zhan Shen (Member, IEEE) received the B.E. degree in electrical engineering and automation from the Nanjing University of Aeronautics and Astronautics, Nanjing, China, in 2013, the M.E. degree in electrical engineering from Southeast University, Nanjing, China, in 2016, the master's degree from RWTH Aachen University, Aachen, Germany, in 2016, and the Ph.D. degree in energy technology from Aalborg University, Aalborg, Denmark, in 2020.

He conducts his research as a Postdoctoral Researcher in Aalborg until 2021 and an Associate Research Fellow with Southeast University. He was a Visiting Student with RWTH Aachen University. He was a Visiting Scholar with the Massachusetts Institute of Technology (MIT), Cambridge, MA, USA, from October 2018 to January 2019. He was with ABB Corporate Research Center, Beijing, China, in 2016. His research interests include the electromagnetic-thermal-reliability modeling and design of magnetic components in power electronic converters, and EMI.

Yichen Chen was born in Zhejiang, China, in 1997. He received the B.S. degree in electrical engineering and its automation from the Changchun University of Science and Technology, Jilin, China, in 2020. He is currently working toward the M.S. degree in electrical engineering with Southeast University, Nanjing, China.

His research interests include *LLC* resonant converter optimization and high-power high-frequency transformer design.

Long Jin received the master's degree in automation and the Ph.D. degree in vibration, concussion, and noises from the Nanjing University of Aeronautics and Astronautics, Nanjing, China, in 1993 and 1997, respectively.

He is currently a Professor with the School of Electrical Engineering, Southeast University, Nanjing. His current research interests include the design and control of high-power electronics, ultrasonic motors, and robotics.

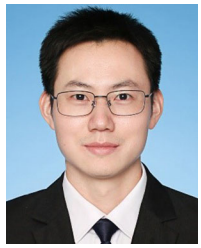

Dajun Ma (Student Member, IEEE) was born in Anhui, China, in 1993. He received the B.S. and M.S. degrees in electrical engineering from Anhui University, Hefei, China, in 2014 and 2017, respectively. He is currently working toward the Ph.D. degree in electrical engineering with Southeast University, Nanjing, China.

His current research interests include power electronic transformers and multiport converters for the ac/dc hybrid system.

Biao Zou was born in Longyan, Fujian, China, in 1968. He received the B.S. degree in electronic engineering from Tianjin University, Tianjin, China, in 1989.

Since 1989, he has been working with Fujian Longking Co., Ltd.. He is a Senior Engineer and Vice Minister of electrical control division. His research interests include high voltage power supply for electrostatic precipitator, and electric control system of flue gas desulfurization and flue gas denitration.